INTERNATIONAL JOURNAL OF CIRCUIT THEORY AND APPLICATIONS
*Int. J. Circ. Theor. Appl.* (2016)

# 67 GHz three-spiral transformer CMOS oscillator

Domenico Pepe[1], Ilias Chlis[1,2] and Domenico Zito[1,2,*,†]

[1] *Marconi Lab, Micro & Nano Systems Centre, Tyndall National Institute, Dyke Parade, Cork, Ireland*
[2] *Electrical and Electronic Engineering, School of Engineering, University College Cork, College Road, Cork, Ireland*

## SUMMARY

This paper presents a 67GHz LC oscillator exploiting a three-spiral transformer and implemented in 65nm bulk complementary metal–oxide–semiconductor technology by STMicroelectronics. The three-spiral transformer allows operating with a lower voltage supply, still obtaining good phase noise performance, and achieving a compact design. Measured performances when supplied with 1.2 V are: oscillation frequency of 67 GHz, phase noise (*PN*) equal to −96 dBc/Hz at 1 MHz frequency offset from the carrier, power consumption ($P_C$) equal to 19.2 mW and figure of merit (*FOM*) equal to −179.7 dB/Hz. Measured performances when supplied with 0.6 V are: oscillation frequency of 67 GHz; *PN* equal to −88.7 dBc/Hz at a 1 MHz frequency offset from the carrier; $P_C$ equal to 3.6 mW and *FOM* equal to −179.7 dB/Hz. Copyright © 2016 John Wiley & Sons, Ltd.

Received 9 July 2015; Revised 18 December 2015; Accepted 21 December 2015

KEY WORDS: CMOS, mm-wave; oscillator; transformer

## 1. INTRODUCTION

In the last few years, the interest in millimetre-wave (mm-wave) wireless systems has grown consistently. Examples of the most attractive applications for mm-wave wireless systems are 60 GHz multi-gigabit-per-second wireless communications [1, 2], 77–79 GHz automotive radars [3, 4] and W-band passive imaging [5].

This paper presents a 67 GHz oscillator implemented in 65 nm complementary metal–oxide–semiconductor (CMOS) technology by STMicroelectronics. The oscillator exploits the topology we introduced in [6]. This topology exploits a three-spiral transformer in order to achieve low power consumption ($P_C$), good phase noise (PN, [7]) and a compact design. With respect to [6], we report here for the first time the test-chip realization in 65 nm CMOS, the theoretical circuit analysis with the analytical expressions of oscillation frequency, startup condition, loop gain, output voltage, effective quality factor ($Q$) of the tank, the complete theoretical analysis of phase noise (validated through the comparison with the results of the circuit simulations carried out within the Cadence design environment), the description of the measurement setup and the experimental results of the test-chip characterization.

The paper is organized as follows. Section 2 reports the operating principle of the three-spiral transformer oscillator. Section 3 reports the theoretical circuit analysis and the derivation of the open-loop transfer function, oscillation frequency, oscillation startup condition, output voltage, equivalent quality factor of the tank and phase noise. Section 4 reports the oscillator circuit design in 65-nm bulk CMOS technology by STMicroelectronics. Section 5 reports the experimental results. Finally, in Section 6, conclusions are drawn.

---

*Correspondence to: Domenico Zito, Electrical and Electronic Engineering, School of Engineering, University College Cork, and Tyndall National Institute, Cork, Ireland.
[†] E-mail: domenico.zito@tyndall.ie

## 2. OPERATING PRINCIPLE

The schematic of the proposed mm-wave oscillator is shown in Figure 1. It consists of a cross-coupled topology with a three-spiral transformer. The first mutual coupling is between the two spirals of the tank ($L_{D1}$ and $L_{D2}$). By coupling the two spirals with the drain voltages in opposition of phase, the voltage amplitude across the spiral is enhanced and the oscillation is boosted, leading to higher amplitude of the output oscillation and thereby better phase noise [8].

The inductance seen from the drain terminals of the transistors is increased by the amount approximately equal to $M_1 \times |i_{D1}/i_{D2}| \approx M_1$, where $M_1$ is the mutual inductance between the two spirals ($M_1 = k_1\sqrt{L_{D1}L_{D2}}$, $k_1$ is the coupling factor), and $i_{D1}$ and $i_{D2}$ are the currents in $L_{D1}$ and $L_{D2}$. The parasitic resistance of the spirals is unchanged, thereby allowing an increase of the effective quality factor ($Q$) [9] of the tank.

The transformer feedback between drain and source spirals ($L_{D1}$–$L_{S1}$ and $L_{D2}$–$L_{S2}$, Figure 1) also allows the drain and source voltages to swing above the supply voltage and below ground, respectively; moreover, drain and source nodes oscillate in phase, as reported in [10].

## 3. CIRCUIT ANALYSIS

The oscillator shown in Figure 1 can be represented as in Figure 2(a), where $R_D$, $R_S$, $C_D$ and $C_S$ are the resistances and capacitances seen at the drain and source nodes, respectively, of the transistor pair $M_{C1,2}$. Both $L_{D1}$ and $L_{D2}$ are equal to $L_D$, whereas both $L_{S1}$ and $L_{S2}$ are equal to $L_S$.

The half-circuit equivalent model is shown in Figure 2(b). $L_{DM}$ takes into account the increase of inductance because of the mutual coupling between the two spirals at the drain node, $L_D$. If we consider $k_1$ equal to one (actual values are lower), then $L_{DM} = L_D$.

The open-loop transfer function, oscillation frequency and startup condition are derived in Subsection 3.1. The analytical expression for the oscillation voltage is provided in Subsection 3.2. In Subsection 3.3, the expression for the equivalent quality factor of the tank is derived. In Subsection 3.4, the expression of the phase noise is provided and the analytical results are compared with the simulation results.

### 3.1. *Open-loop transfer function, oscillation frequency and startup condition*

The open-loop transfer function, $H(s)$, can be derived from the circuit of Figure 2(b), as follows:

$$H(s) = \frac{V_{\mathrm{OUT}}(s)}{V_{\mathrm{IN}}(s)} = \left(\frac{V_{\mathrm{OUT}}(s)}{V_X(s)}\right)^2 \qquad (1)$$

where $s = j\omega$, $\omega$ being the angular frequency, and $V_{OUT}/V_X = V_X/V_{IN}$.

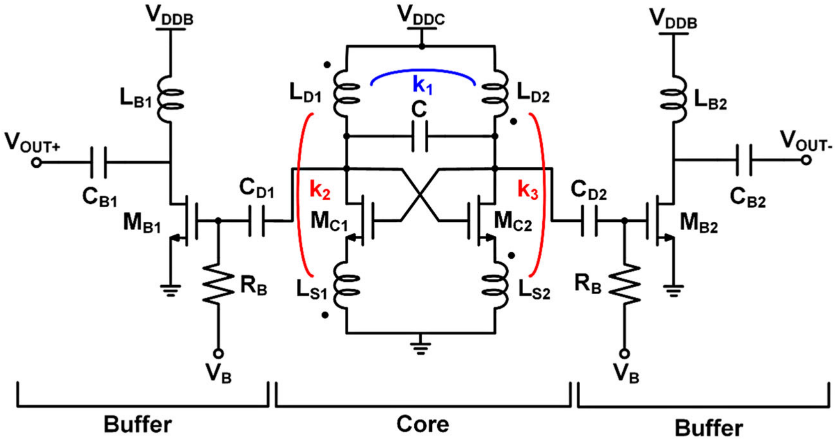

Figure 1. Schematic of the three-spiral transformer oscillator.

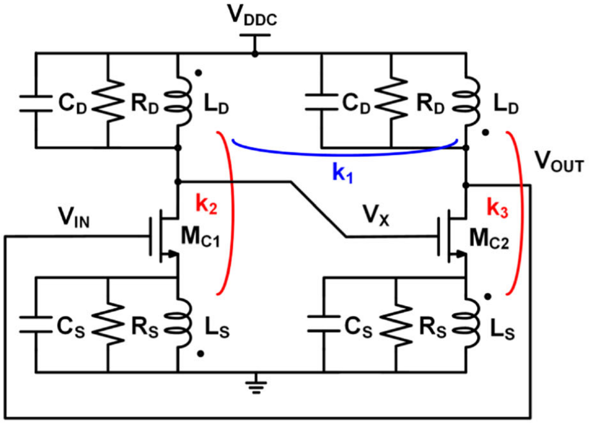

(a)

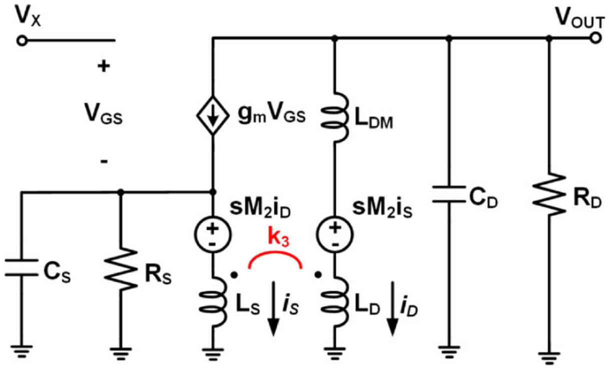

(b)

Figure 2. (a) Equivalent circuit of the oscillator; (b) half circuit equivalent model.

Let us call $Z_D$ the parallel impedance of $R_D$ and $C_D$ and $Z_S$ the parallel impedance of $R_S$ and $C_S$, expressed as

$$Z_D = \frac{R_D}{1 + sC_D R_D} \tag{2}$$

$$Z_S = \frac{R_S}{1 + sC_S R_S} \tag{3}$$

By considering the Kirchhoff's current law at the drain and source terminals, respectively,

$$g_m V_{GS} + \frac{V_{\mathrm{OUT}}}{Z_D} + I_D = 0 \tag{4}$$

$$\frac{V_X - V_{GS}}{Z_S} - g_m V_{GS} + I_S = 0 \tag{5}$$

and expressing the drain voltage ($V_{OUT}$) and source voltage ($V_X - V_{GS}$), respectively,

$$V_{\mathrm{OUT}} = (L_D + L_{DM})sI_D + I_S M_2 s \tag{6}$$

$$V_X - V_{GS} = L_S s I_S + I_D M_2 s \tag{7}$$

where $M_2 = k_3\sqrt{L_S L_D}$, we can derive the expressions of $V_{GS}$, by substituting (4) and (5) in (6), and $V_X$, by substituting (4) and (5) in (7),

$$V_{GS} = \frac{\frac{M_2 s}{Z_S} V_X + V_{\mathrm{OUT}}\left(1 + \frac{L_D + L_{DM}}{Z_D} s\right)}{-(L_D + L_{DM}) s g_m + g_m M_2 s + \frac{M_2 s}{Z_S}} \tag{8}$$

$$V_X = \frac{1}{1 + \frac{L_S s}{Z_S}}\left(1 + L_S s g_m + \frac{L_S s}{Z_S} - g_m M_2 s\right) V_{GS} - \frac{1}{1 + \frac{L_S s}{Z_S}} \frac{M_2 s}{Z_D} V_{\mathrm{OUT}} \tag{9}$$

Then, considering $k_{1,3}$ as unity and by substituting (8) and (9) in (1), we obtain the open-loop transfer function as expressed by (10),

$$H(s) = \left[\frac{s^3 \alpha C_S L_S L_D g_m + s^2 \alpha \frac{L_S L_D g_m}{R_S} + s g_m\left(L_D + L_S - 2\sqrt{L_S L_D} + \alpha L_D\right)}{s^4 \alpha C_S C_D L_S L_D + s^3 \alpha L_S L_D\left(g_m C_D + \frac{C_S}{R_D} + \frac{C_D}{R_S}\right) + s^2 \alpha\left[C_S L_S + 2 C_D L_D + L_S L_D\left(\frac{g_m}{R_D} + \frac{1}{R_S R_D}\right)\right] + s\left[\alpha\left(\frac{L_S}{R_S} + 2\frac{L_D}{R_D}\right) + g_m L_S\left(\sqrt{\frac{L_D}{L_S}} + \alpha - 1\right)\right] + \alpha}\right]^2 \tag{10}$$

where

$$\alpha = \sqrt{\frac{L_S}{L_D}} - 1 \tag{11}$$

According to the Barkhausen criterion, the circuit oscillates at the oscillation angular frequency $\omega_0$ if $|H(j\omega_0)| = 1$ and $\angle H(j\omega_0) = 0°$. If $H(s = j\omega)$ is written as follows

$$H(s) = \frac{X_N + jY_N}{X_D + jY_D} \tag{12}$$

where $X_N$ and $Y_N$ are the real and imaginary parts of the numerator of $H(s)$ and $X_D$ and $Y_D$ are the real and imaginary parts of the denominator of $H(j\omega)$, the condition on the phase is verified if

$$\frac{X_N}{Y_N} = \frac{X_D}{Y_D} \tag{13}$$

thus

$$X_N Y_D - X_D Y_N = 0 \tag{14}$$

Solving (14) leads to the expression of the oscillation frequency:

$$\omega_0 \approx \sqrt{\frac{1 + R_S g_m + R_D R_S\left(\frac{C_S}{L_D} + \frac{4C_D}{L_S} - \frac{C_D\sqrt{L_D L_S}}{L_D L_S}\right) + A}{2 C_D C_S R_D R_S}} \tag{15}$$

where

$$A = \sqrt{1 + 2R_S g_m + \frac{R_D^2 R_S^2}{L_D^2 L_S^4}\left[\left(C_D\sqrt{L_D} + C_S\sqrt{L_S}\right)^2 + C_D L_D\left(-4C_S + \frac{8L_D}{R_D}\left(\frac{1}{R_S} + g_m\right) - \frac{2\sqrt{L_D L_S}}{R_S}\left(\frac{1}{R_D} - g_m\right)\right) + L_D L_S\left(\frac{L_D g_m^2}{R_D^2} + \frac{2C_S}{R_D R_S} + \frac{2C_S g_m}{R_D}\right)\right]} \tag{16}$$

Figure 3 reports the plot of the oscillation frequency $f_0$ ($f_0 = \frac{\omega_0}{2\pi}$) according to (15) versus $L_S$ and $L_D$, for $g_m = 15$ mS and $C_S = C_D = 150$ fF (values extracted by post-layout simulations of the circuit design), and a quality factor of $L_S$ and $L_D$ equal to 10. As expected, the oscillation frequency increases for lower values of $L_S$ and $L_D$.

A simpler, less accurate, but more intuitive expression of the oscillation frequency can be obtained in case of approximation with ideal tanks ($R_S$ and $R_D$ infinite)

DOI: 10.1002/cta

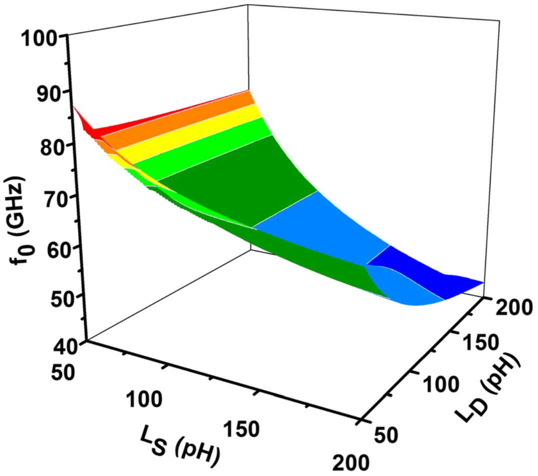

Figure 3. Oscillation frequency, according to (15), versus $L_S$ and $L_D$, for $g_m = 15\,\mathrm{mS}$ and $C_S = C_D = 150\,\mathrm{fF}$, and a quality factor of $L_S$ and $L_D$ equal to 10.

$$\omega_0 \approx \sqrt{\frac{2C_D L_D + C_S L_S + \sqrt{4C_D^2 L_D^2 + C_S^2 L_S^2}}{2C_D C_S L_D L_S}} \tag{17}$$

Last, by imposing $|H(j\omega)| \geq 1$, we derive the oscillation startup condition as follows:

$$g_m R_D \geq \left| R_D \frac{2j\frac{L_D\omega}{R_D}(1 + j\omega C_D R_D) + \frac{\omega L_S}{R_S}(1 + \omega C_S R_S) - \frac{\omega^2 L_D L_S}{R_D R_S}(1 + j\omega C_D R_D)(1 + j\omega C_S R_S) + 1}{-2j\omega L_D - j\omega L_S + 2j\omega\sqrt{L_D L_S} + \frac{\omega^2 L_D L_S}{R_D}(1 + j\omega C_D R_D) + \frac{\omega^2 L_D L_S}{R_S}(1 + j\omega C_S R_S)} \right| \tag{18}$$

### *3.2. Oscillation voltage*

In order to derive an analytical expression for the oscillation voltage at the drain node of $M_{C1,2}$, the drain current is approximated by its fundamental component ($I_{\omega 0}$), with $I_{\omega 0}$ equal to $\frac{2}{\pi} I_{DC}$, where $I_{DC}$ is the average current consumed by the oscillator. Assuming that the drain and source currents of the transistor pair $M_{C1,2}$ are equal, (4) and (5) can be rewritten respectively as follows

$$I_{\omega 0} + \frac{V_{\mathrm{OUT}}}{Z_D} + I_D = 0 \tag{19}$$

$$-I_{\omega 0} + \frac{V_S}{Z_S} + I_S = 0 \tag{20}$$

where $V_S$ is the voltage at the source of transistor pair $M_{C1,2}$.

Moreover,

$$V_S = L_S s I_S + I_D M_2 s \tag{21}$$

Combining (20) and (21), we find

$$I_S = \frac{Z_S}{Z_S + sL_S} I_{\omega 0} - \frac{M_2 s}{Z_S + sL_S} I_D \tag{22}$$

Then, substituting $I_D$ and $I_S$ in (6), with the derived expressions from (19) and (22), respectively, we find

$$V_{\mathrm{OUT}} = Z_D s \frac{-(L_D + L_{DM})(Z_S + sL_S) + M_2(Z_S + M_2 s)}{(Z_S + sL_S)[Z_D + s(L_D + L_{DM})] - M_2^2 s^2} I_{\omega 0} \tag{23}$$

which, by considering $k_{1,3}$ as unity, can be rewritten as in (24).

$$V_{\mathrm{OUT}} = -\frac{\frac{C_S L_S L_D}{R_D} s^3 + \frac{L_S L_D}{R_S R_D} s^2 + \frac{2L_D - \sqrt{L_S L_D}}{R_D} s}{C_S C_D L_S L_D s^4 + L_S L_D \left(\frac{C_S}{R_D} + \frac{C_D}{R_S}\right) s^3 + \left(C_S L_S + 2C_D L_D + \frac{L_S L_D}{R_S R_D}\right) s^2 + \left(\frac{L_S}{R_S} + 2\frac{L_D}{R_D}\right) s + 1} I_{\omega 0} R_D \tag{24}$$

Finally, assuming $I_{\omega 0} R_D = \frac{2}{\pi} I_{DC} R_D \approx V_{DD}$, from (23) and (24), it can be noted that by means of a proper selection of $L_S$ and $L_D$ (and their quality factor), the maximum oscillation amplitude can be higher than $2V_{DD}$ [11].

Figure 4(a)–(d) shows $V_{\mathrm{OUT}}$, according to (24), versus $L_S$ and $L_D$, for $V_{DD}$ equal to 0.6 and 1.2 V, at $f_0 = 67$ GHz, for $g_m = 15$ mS and $C_S = C_D = 150$ fF, and a quality factor of $L_S$ and $L_D$ equal to 10. It is worth mentioning that the higher the quality factor of $L_S$ and $L_D$, the higher is the resulting $V_{\mathrm{OUT}}$.

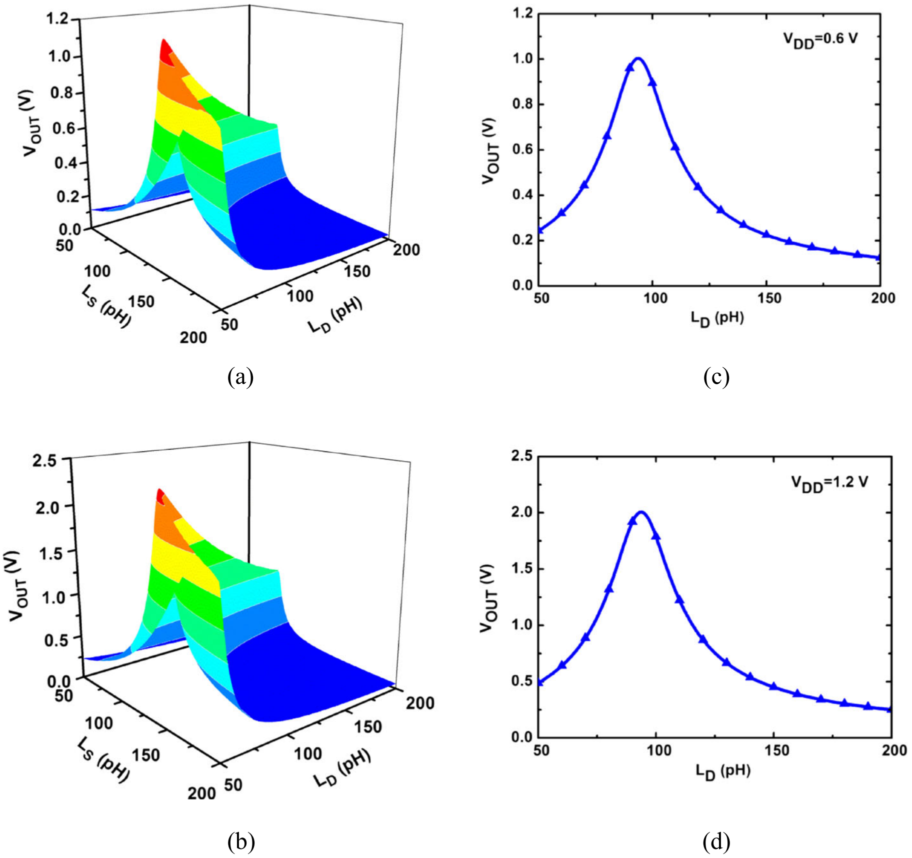

(a) (c)

(b) (d)

Figure 4. Oscillation amplitude at the drain of $M_C$ ($V_{\mathrm{OUT}}$) versus $L_S$ and $L_D$, for $V_{DD}$ equal to (a) 0.6 and (b) 1.2 V, at $f_0 = 67$ GHz, for $g_m = 15$ mS and $C_S = C_D = 150$ fF, and a quality factor of $L_S$ and $L_D$ equal to 10. Oscillation amplitude at the drain of $M_C$ ($V_{\mathrm{OUT}}$) versus $L_D$ for a value of $L_S = 100$ pH, for $V_{DD}$ equal to (c) 0.6 and (d) 1.2 V.

### 3.3. *Equivalent quality factor of the tank*

In order to show that the magnetic coupling between $L_{D1}$ and $L_{D2}$ leads to an effective enhancement of the quality factor of the LC tank in the oscillator circuit of Figure 1, a closed-form expression for $Q$ is derived hereinafter. $Q$ is calculated from the open-loop transfer function (10) as follows:

$$Q = \left| \frac{\omega}{2} \frac{d\angle H(j\omega)}{d\omega} \right| \tag{25}$$

where $\angle H(j\omega)$ is the phase of the open-loop transfer function $V_{\mathrm{OUT}}/V_{\mathrm{IN}}$

$$\angle H(j\omega) = 2\left[\tan^{-1}\frac{\omega(-A\omega^2 + C)}{-B\omega^2} - \tan^{-1}\frac{\omega(-E\omega^2 + G)}{D\omega^4 - F\omega^2 + 1}\right] \tag{26}$$

Where, for $k_{2,3}$ approaching unity,

$$A = -\, C_S L_S L_{DM} g_m \tag{27}$$

$$B = -\frac{L_S L_{DM} g_m}{R_S} \tag{28}$$

$$C = -g_m\left(L_D - \sqrt{L_D L_S} + L_{DM}\right) \tag{29}$$

$$D = C_D C_S L_S L_{DM} \tag{30}$$

$$E = L_S L_{DM}\left(\frac{C_D}{R_S} + \frac{C_S}{R_D} + C_D g_m\right) \tag{31}$$

$$F = \frac{L_S L_{DM}}{R_D R_S} + C_D L_D + C_D L_{DM} + C_S L_S + \frac{L_S L_{DM} g_m}{R_D} \tag{32}$$

$$G = \frac{L_D}{R_D} + \frac{L_S}{R_S} + \frac{L_{DM}}{R_D} + L_S g_m - g_m\sqrt{L_D L_S} \tag{33}$$

$Q$ can be rewritten as

$$Q = \omega\left|\frac{(-3A\omega^2 + C)(-B\omega^2) + (-A\omega^2 + C)2B\omega^2}{(-B\omega^2)^2 + \omega^2(-A\omega^2 + C)^2)} - \frac{(-3E\omega^2 + G)(D\omega^4 - F\omega^2 + 1) - \omega^2(-E\omega^2 + G)(4D\omega^2 - 2F)}{(D\omega^4 - F\omega^2 + 1)^2 + \omega^2(-E\omega^2 + G)^2}\right| \tag{34}$$

that is, at the oscillation frequency $f_0$, equal to about $2(1+k_1)\times Z$, where $Z$ is a constant dependent on the circuit elements. The factor 2 is due to the cascade of frequency-selective stages that makes the phase transition sharper than that of a single stage.

Figure 5 reports a three-dimensional plot of the equivalent $Q$ of the LC tank for the cross-coupled oscillator circuit of Figure 1, with respect to $L_{D1,2} = L_{S1,2} = L$ and the oscillation frequency $f_0$, with the assumption that the quality factor of the transformer spirals ($Q_{D1,2}$ and $Q_{S1,2}$, quality factors of the inductors $L_{D1,2}$ and $L_{S1,2}$, respectively) is equal to 10 and the coupling coefficients $k_{1,2,3}$ are equal to 1. We observe that, at $f_0 = 67\,\mathrm{GHz}$ and for $L \approx 40\,\mathrm{pH}$, the LC tank $Q$ is equal to about

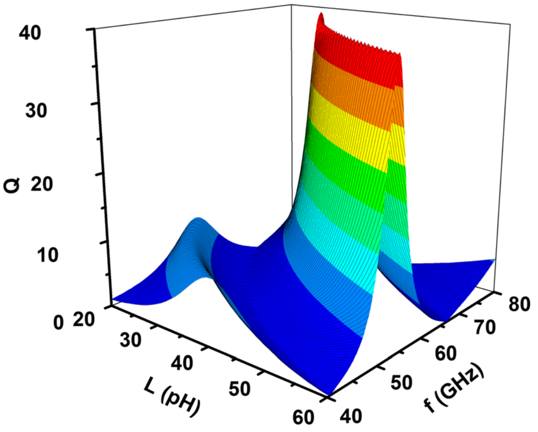

Figure 5. Three-dimensional plot of the equivalent quality factor ($Q$) of the LC tank for the oscillator circuit of Figure 1, with respect to $L_{D1,2} = L_{S1,2} = L$ and the oscillation frequency $f_0$, assuming $Q_{D1,2} = Q_{S1,2} = 10$ and $k_{1,2,3} = 1$.

$2 \times (1 + k_1) \times Q_{D1,2} = 40$. Thereby, the magnetic coupling between $L_{D1}$ and $L_{D2}$ enhances the effective quality factor of the LC tank up to $1 + k_1$ times. This is an important result because the realization of high $Q$ inductors at the mm-waves is challenging, because of loss mechanisms in the silicon substrate [12]. Moreover, in ultra-scaled technology nodes, it is even more difficult to achieve high quality factors, because of the reduced thickness of the metal layers. Thereby, the differential cross-coupled oscillator circuit shown in Figure 1 shows a potential for achieving a better spectral purity beyond the limited quality factor of the integrated inductors.

### 3.4. *Phase noise*

The phase noise is typically the most important performance parameter for an oscillator [13–15]. In this section, the phase noise expressions for the oscillator of Figure 1 are derived, both for the $1/f^3$ and $1/f^2$ phase noise regions. The analytical expressions of phase noise due to flicker and thermal noise sources are validated by the results obtained through SpectreRF simulations for the oscillation frequency of 67 GHz.

Assuming that the losses due to the parasitic resistance of the inductors $L_D$ and $L_S$ dominate the losses in the drain and source resonators, the parasitic resistors $R_D$ and $R_S$ in parallel to $L_D$ and $L_S$ are equal to $Q_D L_D \omega$ and $Q_S L_S \omega$, respectively, where $Q_D$ and $Q_S$ are the quality factors of the inductors $L_D$ and $L_S$ and $\omega$ is the angular frequency.

We define $\Gamma_{\mathrm{eff,rms}}$ and $\Gamma_{\mathrm{eff,dc}}$ as the rms and dc values of the effective impulse sensitivity function (ISF) for the noise current of $M_{C1,2}$ [8]. Using $\Gamma^2_{\mathrm{eff,rms}}$ in (23) and $\Gamma^2_{\mathrm{eff,dc}}$ in (25) from [8] and equating, we find

$$\Gamma^2_{\mathrm{eff,dc}} = \frac{\omega_{1/f^3}}{\omega_{1/f}} \Gamma^2_{\mathrm{eff,rms}} \tag{35}$$

where $\omega_{1/f^3}$ is the frequency where the sideband power due to thermal noise is equal to the sideband power due to flicker noise, and $\omega_{1/f}$ is the corner frequency of the flicker noise generated by $M_{C1,2}$. From [16], $\mathit{\Gamma}^2_{\mathrm{eff,rms}}$ is given by

$$\Gamma^2_{\mathrm{eff,rms}} = \frac{2 I_B}{\mu_n C_{ox} \frac{W}{L} \pi N^2 V^2_{\mathrm{tank}}} \tag{36}$$

where $N = 2$ for the differential cross-coupled topology, $\mu_n$ is the electron mobility approximately equal to $0.039\,\mathrm{m}^2/(V \times s)$, $C_{ox}$ is the gate oxide capacitance per unit area approximately equal to $0.0163\,\mathrm{F/m}^2$, $W$ and $L$ are the width and length of $M_{C1,2}$, respectively, and $V_{\mathrm{tank}}$ is the peak amplitude of the output voltage $V_{\mathrm{OUT}}$, (24).

The phase noise due to flicker noise from $M_{C1,2}$ can be written as

$$\mathscr{L}(\Delta\omega)|_{\text{flicker}} = N\frac{1}{2q_{\max}^2\Delta\omega^2}\Gamma_{\text{eff,dc}}^2\frac{\overline{i_{n,\text{flicker}}^2}}{\Delta f}\frac{1}{\sin\phi+\sqrt{2\sin^2\Phi-\sin^2\phi}} \tag{37}$$

where the last term takes into account the cyclostationarity of the flicker noise current of $M_{C1,2}$, $\phi$ is equal to $\omega_0 t$, $q_{\max}$ is the maximum charge displacement across the tank capacitance $C_{\text{tank}}$, equal to $V_{\text{tank}}\times C_{\text{tank}}$. $\Delta\omega$ is the angular frequency offset from the oscillation frequency, and $\Phi$ is half the conduction angle defined by

$$\Phi = \sin^{-1}\sqrt{\frac{I_B}{\mu_n C_{ox}\frac{W}{L}V_{\text{tank}}^2}} \tag{38}$$

where $I_B$ is the total bias current. Also, $\overline{i_{n,\text{flicker}}^2}/\Delta f$ is the power spectral density of the flicker noise current of $M_{C1,2}$

$$\frac{\overline{i_{n,\text{flicker}}^2}}{\Delta f} = \frac{Kg_m^2}{C_{ox}WL}\frac{1}{f} \tag{39}$$

where $K$ is a process-dependent constant approximately equal to $10^{-23}\,\text{V}^2\text{F}$, $f$ is the frequency, and $g_m$ is the small-signal transconductance of $M_{C1,2}$ given by

$$g_m = \left(\mu_n C_{ox}\frac{W}{L}\right)V_{\text{tank}}\left(\sin\phi+\sqrt{2\sin^2\Phi-\sin^2\phi}\right) \tag{40}$$

The phase noise due to flicker noise from $M_{C1,2}$, given by (37), can now be rewritten as

$$\mathscr{L}(\Delta\omega)|_{\text{flicker}} = \frac{2KI_B\mu_n}{NC_{\text{tank}}^2V_{\text{tank}}^2L^2}\frac{\omega_{1/f^3}}{\omega_{1/f}}\frac{1}{\Delta\omega^3} \tag{41}$$

Regarding the phase noise due to thermal noise from $M_{C1,2}$ and $R_{D,S}$, it can be written as

$$\mathscr{L}(\Delta\omega)|_{\text{thermal}} = N\frac{1}{2q_{\max}^2\Delta\omega^2}\left(\Gamma_{\text{eff,rms}}^2\frac{\overline{i_{n,\text{thermal}}^2}}{\Delta f}\frac{1}{\sin\phi+\sqrt{2\sin^2\Phi-\sin^2\phi}}+\Gamma_{R_1,\text{rms}}^2\frac{\overline{i_{n,R_D}^2}}{\Delta f}+\Gamma_{R_2,\text{rms}}^2\frac{\overline{i_{n,R_S}^2}}{\Delta f}\right) \tag{42}$$

where, $\overline{i_{n,\text{thermal}}^2}/\Delta f$ and $\overline{i_{n,R_{D,S}}^2}/\Delta f$ are the power spectral densities of the thermal noise currents of $M_{C1,2}$ and $R_{D,S}$, respectively, given by

$$\frac{\overline{i_{n,\text{thermal}}^2}}{\Delta f} = 4K_BT\gamma g_m \tag{43}$$

$$\frac{\overline{i_{n,R_{D,S}}^2}}{\Delta f} = \frac{4K_BT}{R_{D,S}} \tag{44}$$

where $K_B$ is the Boltzmann constant, $T$ is the absolute temperature and $\gamma$ is the excess noise coefficient. From [16], $\Gamma_{R_{1,2},\text{rms}}^2$ is equal to $1/(2N^2)$.

The phase noise due to thermal noise from $M_{C1,2}$ and $R_{D,S}$, given by (42), can now be rewritten as

$$\mathscr{L}(\Delta\omega)|_{\text{thermal}} = \frac{2K_BT}{NC_{\text{tank}}^2 V_{\text{tank}}^2}\frac{1}{\Delta\omega^2}\left(\frac{2I_B\gamma}{\pi V_{\text{tank}}} + \frac{1}{2R_D} + \frac{1}{2R_S}\right) \tag{45}$$

At resonance, $V_{\text{tank}}$ can be approximated by

$$V_{\text{tank}} \approx \frac{2}{\pi} I_B R_{eq} \tag{46}$$

where

$$R_{eq} = 2\pi f_0 L_D Q \tag{47}$$

$$Q = (1 + k_1)Q_D \tag{48}$$

The phase noise expressions due to flicker and thermal noise can be rewritten respectively in terms of $Q_D$ as

$$\mathscr{L}(\Delta\omega)|_{\text{flicker}} = \frac{K\mu_n}{2^3 NC_{\text{tank}}^2 I_B[(1+k_1)L_D f_0 Q_D]^2 L^2}\frac{\omega_{1/f^3}}{\omega_{1/f}}\frac{1}{\Delta\omega^3} \tag{49}$$

$$\mathscr{L}(\Delta\omega)|_{\text{thermal}} = \frac{K_BT}{8NC_{\text{tank}}^2 I_B^2[(1+k_1)L_D Q_D f_0]^2}\frac{1}{\Delta\omega^2}\left[\frac{\gamma}{2\pi(1+k_1)L_D Q_D f_0} + \frac{1}{2R_D} + \frac{1}{2R_S}\right] \tag{50}$$

The coupling between $L_{D1}$ and $L_{D2}$ reduces the phase noise in the $1/f^3$ region by a factor of $(1+k_1)^2=4$ (6 dB), assuming $k_1=1$. Regarding the $1/f^2$ region, the coupling between $L_{D1}$ and $L_{D2}$ lowers by $(1+k_1)^3=8$ (9 dB) the phase noise due to the cross-coupled transistors $M_{C1,2}$, and by $(1+k_1)^2=4$ (6 dB) the phase noise from the resistor noise sources.

The overall phase noise is given by

$$\mathscr{L}(\Delta\omega)|_{\text{total}} = 10\log_{10}\left[\mathscr{L}(\Delta\omega)|_{\text{flicker}} + \mathscr{L}(\Delta\omega)|_{\text{thermal}}\right] \tag{51}$$

Figure 6 shows the phase noise obtained by direct plots from periodic steady state (PSS) and periodic noise circuit simulations in SpectreRF, when the supply is either 1.2 or 0.6 V, for an oscillation

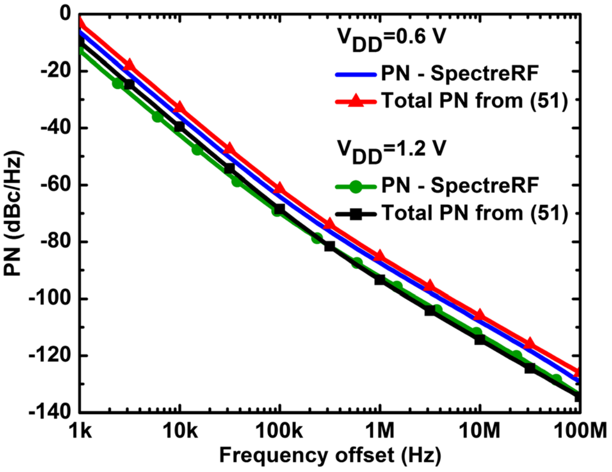

Figure 6. Phase noise (*PN*) versus frequency offset obtained from direct plots through periodic steady state and periodic noise SpectreRF simulations as well as from the theoretical expression (51) for an oscillation frequency of 67 GHz.

DOI: 10.1002/cta

frequency of 67 GHz. Phase noise is reported over a wide frequency offset from the carrier frequency, in order to include the regions in which the noise of the output spectrum is dominated by either flicker or thermal noise contributions.

Figure 6 reports also the numerical evaluation of the theoretical expression of the total phase noise from (51). Note that the theoretical phase noise predicted by (51) matches well with the results obtained by means of SpectreRF simulations. Even at the frequency offset of 100 MHz for $V_{DD}$ equal to 0.6 V, where the worst match is observed, the theoretical phase noise predicted by (51) is within 3.5 dB difference from the simulation results.

## 4. DESIGN IN 65-NM CMOS

The oscillator has been implemented in 65 nm bulk CMOS technology by STMicroelectronics for 67 GHz. The test-chip micrograph is shown in Figure 7.

The chip area is $62 \times 137\,\mu\text{m}^2$ for the core only, and $450 \times 316\,\mu\text{m}^2$ for the overall chip, including buffers and pads. All the transistors are with minimum channel length. $M_C$ and $M_B$ widths are 10 and 20 µm, respectively. The capacitance $C$ in the schematic of Figure 1 consists of the drain parasitic capacitances of the transistors $M_C$. The integrated transformer, inductors, interconnect lines and pads were designed and simulated by means of three-dimensional electromagnetic simulator by Keysight Technologies.

The three-spiral transformer is shown in Figure 8. The transformer has been designed in top metal layer (metal 7) with underpasses in metal 6. The outer diameter is 34.5 µm, and the spacing between the spirals is 0.6 µm. The spiral width is 3.1 µm. The simulation results of the inductance and the quality factor of the integrated spirals are shown in Figure 9(a). Figure 9(b) reports the coupling coefficients

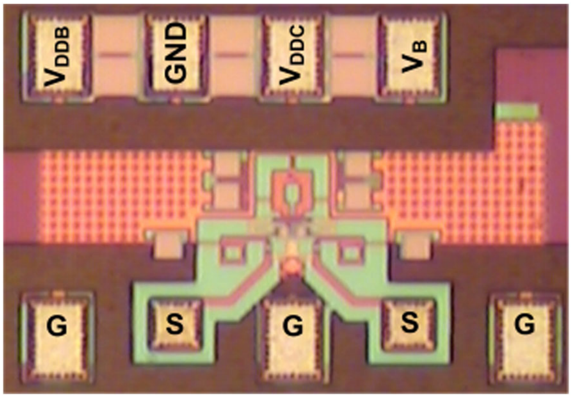

Figure 7. Test-chip micrograph.

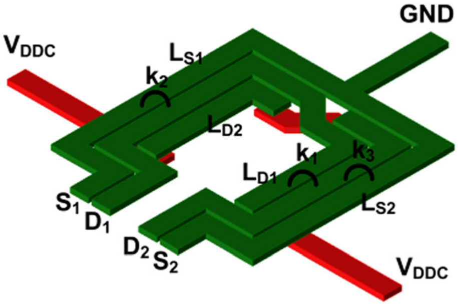

Figure 8. Three-spiral integrated transformer. $D_1/S_1$ and $D_2/S_2$ are the drain/source nodes of transistors $M_{C1}$ and $M_{C2}$, respectively.

DOI: 10.1002/cta

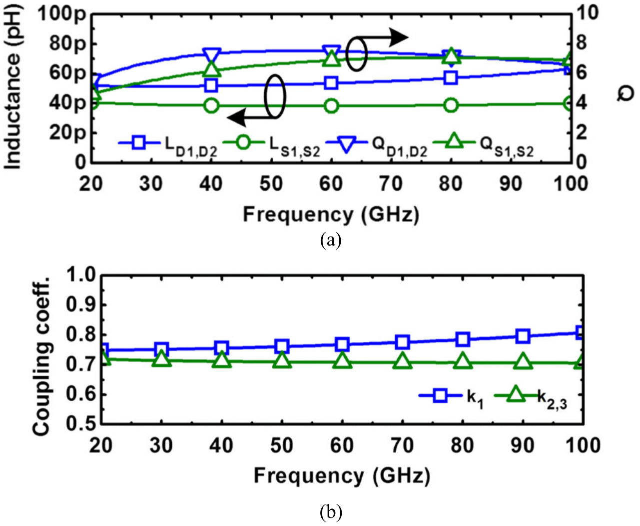

Figure 9. Simulation results of the three-spiral transformer obtained by means of the 3D electromagnetic simulator by Keysight Technologies: (a) inductance values and quality factor of $L_{D1}$, $L_{D2}$, $L_{S1}$ and $L_{S2}$; (b) coupling coefficient between $L_{D1}$ and $L_{D2}$ ($k_1$), as well as between $L_{D1}$–$L_{S1}$ and $L_{D2}$–$L_{S2}$ ($k_2$ and $k_3$, respectively).

between the spirals. The inductors of the buffer are implemented by means of square spirals with outer diameter of 21 µm and width of 3.1 µm. The values at 67 GHz of the inductance, quality factor and coupling factor of the transformer and inductors are reported in Table I.

The transformer design and device placement have been carried out in order to have minimum interconnection lengths. Power, bias and ground are distributed in the circuit through a dense grid made of wide (4 and 5 µm) metal lines in order to minimize parasitic inductances and resistances and to maximize parasitic capacitances, so achieving a more stable ground/bias/power supply and shielding devices and signal lines. Moreover, local decoupling is provided by means of integrated capacitors.

## 5. EXPERIMENTAL RESULTS

The measurement setup is shown in Figure 10(a) and (b). The phase noise and output spectrum of the test-chips were measured by means of an Agilent E5052B signal source analyser connected with an Agilent 5053A microwave downconverter. The cross-correlation technique, which lowers the instrument noise floor by allowing the cancelling of the noise because of the built-in reference sources [17], was used to measure the oscillator phase noise.

On-chip measurements were carried out by means of a 100-µm pitch 40–80 GHz GSGSG Cascade i110 probe with integrated balun in order to convert the differential output signal available from the oscillator to the single-ended signal required for the measurements. The probe is connected to a V-band power divider by means of a 1-mm cable and an Agilent V281D 1-mm coaxial to WR15 waveguide adapter. The outputs of the power divider are connected to a pair of

Table I. Electrical parameters of transformer and inductors at 67 GHz.

| Components | $L$ (pH) | $Q$ | Coupling coefficients | Value |
|---|---|---|---|---|
| $L_{D1}$ and $L_{D2}$ | 54 | 7.4 | $k_1$ | 0.77 |
| $L_{S1}$ and $L_{S2}$ | 38 | 7 | $k_2$ and $k_3$ | 0.71 |
| $L_{B1}$ and $L_{B2}$ | 92 | 14 | | |

DOI: 10.1002/cta

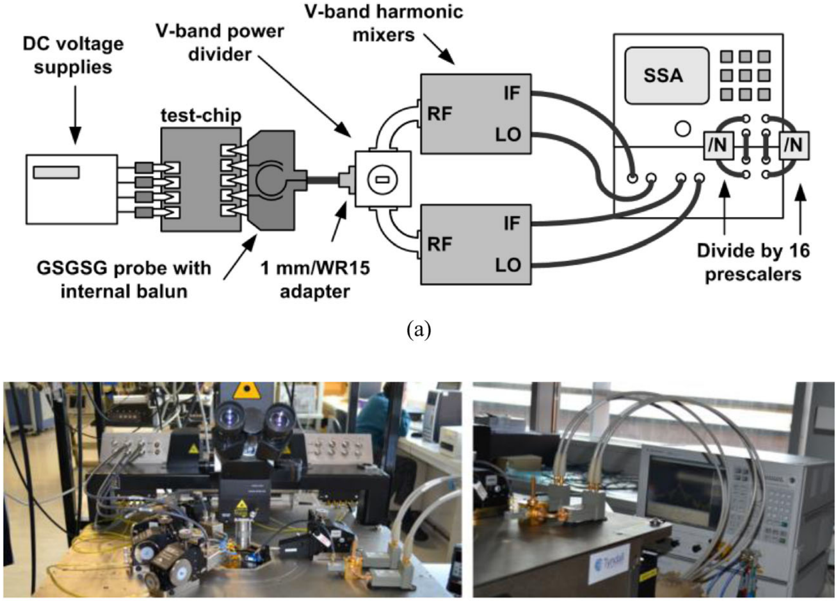

(a)

(b)

Figure 10. Test setup: (a) block diagram and (b) photographs.

V-band Agilent 11970V external harmonic mixers. The external mixers are driven by the E5053A built-in local oscillators.

Free running mm-wave oscillators can cause measurement difficulties because of large frequency drift and high phase noise, such as phase locked loop unlock and/or invalid measurements. Prescaler techniques can help to overcome these difficulties by suppressing both frequency drifts and high phase noise [17]. Two-divide-by-16 prescalers have been used in order to ensure accurate phase noise measurements by means of the E5052B. The visual basic for applications (VBA) macroprogram running on the E5052B automatically corrects the amplitude of the measured phase noise by considering the dividing number of the prescalers.

Measured phase noise and output spectrum are shown in Figure 11(a) and (b). The test-chip exhibits an oscillation at 67 GHz. When biased with 1.2 V, the measured phase noise is equal to −96 dBc/Hz at a 1 MHz frequency offset from the carrier. The $P_C$ amounts to 19.2 mW. When biased with 0.6 V, the oscillator exhibits a phase noise (*PN*) equal to −88.7 dBc/Hz at a 1 MHz frequency offset from the carrier. The power consumption amounts to 3.6 mW. These results have been also confirmed by measurements without prescalers. The figure of merit (*FOM*) [18]

$$FOM = PN \; - \; 20\ \mathrm{Log}\left(\frac{f_0}{\Delta f}\right) + 10\ \mathrm{Log}\left(\frac{P_C}{1\ \ \mathrm{mW}}\right) \tag{52}$$

where $\Delta f$ is the frequency offset and $P_C$ the power consumption in megawatts ($P_C = V_{DD} \times I_C$), amounts to −179.7 dB/Hz for both supply voltages of 1.2 and 0.6 V. It is worth noting that there is no FOM degradation by halving the supply voltage from 1.2 to 0.6 V.

A summary of the performance achieved by the proposed oscillator and a comparison with the state-of-the-art solutions for 60 GHz CMOS oscillators are reported in Table II. This oscillator exhibits the lowest area, one of the lowest power consumptions ($P_C$) and a competitive FOM, with respect to the state of the art. To summarize, the advantages of this circuit topology and design are as follows: (1) the higher equivalent quality factor of the tank and (2) higher output voltage because of the transformer feedbacks that improve the phase noise performance even with reduced supply voltage; and (3) the three-spiral transformer floor plan that allows the implementation in a compact silicon area.

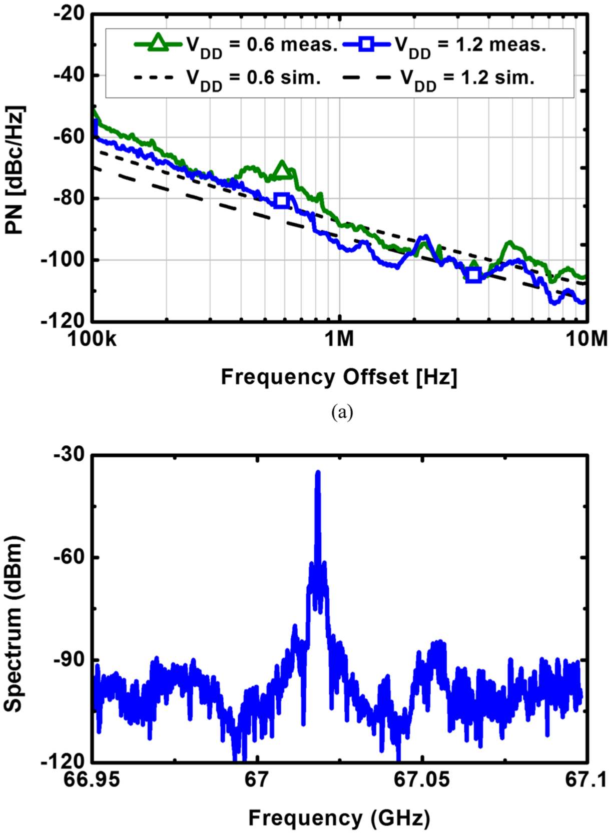

(a)

(b)

Figure 11. Measurement results: (a) phase noise and (b) spectrum.

Table II. Summary of performance and comparison with the state of the art.

| Ref. | Tech. (nm) | Chip area ($mm^2$) | $V_{DD}$ (V) | Freq. (GHz) | *PN* at offset freq. (dBc/Hz) | $P_C$ (mW) | *FOM* |
|---|---|---|---|---|---|---|---|
| [19] | 65 | — | 1–1.2 | 61 | −115 at 10 MHz | 20 | −179.7 |
| [20] | 90 | 0.088 | 0.6 | 64 | −95 at 1 MHz | 3.16 | −185.0 |
| [21] | 90 | 0.034 | 0.6 | 57.6 | −102 at 1 MHz | 7.2 | −189 |
| [22] | 65 | 0.075 | 1 | 58.2 | −95 at 1 MHz | 22 | −177 |
| [23] | 45 | — | 1.1 | 61.6 | −75 at 1 MHz | 28 | −156 |
| [24] | 130 | 0.17 | 1.4 | 52.4 | −97.1 at 1 MHz | 33.6 | −176.2 |
| [25] | 40 | 0.33 | — | 50.72 | −101.8 at 1 MHz | 24 | −182.1 |
| [26] | 65 | 0.032 | 1 | 54 | −95 at 1 MHz | 24 | −179.8 |
| [27] | 130 | 0.24* | 1.5 | 59 | −89 at 1 MHz | 9.8 | −174.5 |
| This work | 65 | 0.008/0.14* | 0.6 | 67 | −88.7 at 1 MHz | 3.6 | −179.7 |
|  |  |  | 1.2 |  | −96 at 1 MHz | 19.2 |  |

*Including buffers and pads.

## 6. CONCLUSIONS

A 67-GHz oscillator circuit was designed and implemented in 65 nm CMOS technology by STMicroelectronics and characterized experimentally. The circuit topology exploits a three-spiral transformer in order to allow low voltage operation and low power consumption, achieving good phase noise and compact design. The expressions of oscillation frequency, startup condition, loop gain, output voltage, equivalent quality factor ($Q$) of the tank and the complete theoretical analysis of phase noise (validated through the comparison with the results of the circuit simulations carried out within the Cadence design environment) have been derived, showing the performance improvements offered by this topology.

The measurements on test-chip show an oscillation frequency of 67 GHz. The oscillator exhibits a phase noise of −96 dBc/Hz at a 1 MHz frequency offset from the carrier, a power consumption of 19.2 mW and a figure of merit of −179.7 dB/Hz when supplied with 1.2 V. When supplied with 0.6 V, it exhibits a phase noise of −88.7 dBc/Hz at a 1 MHz frequency offset from the carrier, a power consumption of 3.6 mW and the same figure of merit (−179.7 dB/Hz), that is, with no degradation with respect to the case with 1.2 V supply voltage. This design exhibits the lowest area occupancy, lowest voltage supply and a competitive figure of merit compared with the state of the art for CMOS oscillators in the 60 GHz band.

## ACKNOWLEDGEMENTS

This work was supported by Irish Research Council (IRC), Science Foundation Ireland (SFI), SFI/EI Technology Innovation Development Award (TIDA), Higher Education Authority (HEA) and Keysight Technologies. This publication has emanated also from research supported in part by a research grant from Science Foundation Ireland (SFI) and is co-funded under the European Regional Development Fund under grant number 13/RC/2077.

## REFERENCES

1. Niknejad A. 0–60 GHz in four years: 60 GHz RF in digital CMOS. *IEEE Solid-State Circuits Newsletter* 2007; **12**(2):5–9.
2. Pepe D, Zito D. System-level simulations investigating the system-on-chip implementation of 60-GHz transceivers for wireless uncompressed HD video communications. Chapter 9 of book. In *Applications on Matlab in Science and Engineering*. InTech Publisher: Rijeka, Croatia, 2011; 181–196.
3. Schneider M. Automotive radar – status and trends. *German Microwave Conference GeMiC 2005*, Ulm, Germany, 2005; 144–147.
4. Nicolson ST, Yau KHK, Pruvost S, Danelon V, Chevalier P, Garcia P, Chantre A, Sautreuil B, Voinigescu SP. A low-voltage SiGe BiCMOS 77-GHz automotive radar chipset. *IEEE Transaction on Microwave Theory and Techniques* 2008; **56**(5):1092–1104.
5. Mereni LO, Pepe D, Zito D. Feasibility study of 95-GHz SoC CMOS radiometers for passive body imaging. *Analog Integrated Circuits and Signal Processing – Special Issue on ICECS 2012* 2013; **77**(3):373–383.
6. Pepe D, Zito D. 0.4 V Low-power 60-GHz oscillator in 65 nm CMOS. *19th IEEE Int. Conf. on Electronics*, *Circuits and Systems* (*ICECS*), 2012; 789–792.
7. Chlis I, Pepe D, Zito D. Analyses and techniques for phase noise reduction in CMOS Colpitts oscillator topology. *International Journal of Circuit Theory and Applications* 2015. doi:10.1002/cta.2097.
8. Hajimiri A, Lee TH. Oscillator phase noise: a tutorial. *IEEE Journal of Solid-State Circuits* 2000; **35**(3):326–336.
9. Pepe D, Zito D. 50 GHz mm-wave CMOS active inductor. *IEEE Microwave and Wireless Components Letters* 2014; **24**(4):254–256.
10. Kwoch K, Luong H-C. Ultra-low-voltage high-performance CMOS VCOs using transformer feedback. *IEEE Journal of Solid-State Circuits* 2005; **40**(3):652–660.
11. Yang J, Kim C-Y, Kim D-W, Hong S. Design of a 24-GHz CMOS VCO with an asymmetric-width transformer. *IEEE Transaction on Circuits and Systems II: Express Briefs* 2010; **57**(3):173–177.
12. Aluigi L, Alimenti F, Pepe D, Roselli L, Zito D. MIDAS: automated approach to design microwave integrated inductors and transformers on silicon. *Radioengineering* 2013; **22**(3):714–723.
13. Pankratz E, Sánchez-Sinencio E. Survey of integrated-circuit-oscillator phase-noise analysis. *International Journal of Circuit Theory and Applications* 2014; **42**:871–938.
14. Buonomo A, Schiavo AL. Modelling and analysis of differential VCOs. *International Journal of Circuit Theory and Applications* 2004; **32**:117–131.
15. Nikpaik A, Nabavi A. Analysis of flicker noise conversion to phase noise in CMOS differential LC oscillators. *International Journal of Circuit Theory and Applications* 2015. doi:10.1002/cta.2083.
16. Andreani P, Wang X, Vandi L, Fard A. A study of phase noise in Colpitts and LC-tank CMOS oscillators. *IEEE Journal of Solid-State Circuits* 2005; **40**(5):1107–1118.
17. Making phase-noise measurement above 26.5 GHz. Agilent E5052B Signal Source Analyzer Help, [Online]. (Available: http://ena.support.keysight.com/e5052b/manuals/webhelp/eng/measurement_using_e5053a_and_external_mixer/making_phase_noise_measurement_above_26_5_ghz.htm)
18. Zito D, Fonte A, Pepe D. 13 GHz CMOS active inductor LC VCO. *IEEE Microwave and Wireless Components Letter* 2012; **22**(3):138–140.
19. Vecchi F, Bozzola S, Pozzoni M, Guermandi D, Temporiti E, Repossi M, Decanis U, Mazzanti A, Svelto F. A wideband mm-wave CMOS receiver for GB/s communications employing interstage coupled resonators. *IEEE Int. Solid-State Circuit Conference*, 2010; 220–221.

20. Li L, Reyneart P, Steyeart M. A low power mm-wave oscillator using power matching techniques. *IEEE Radio Frequency Integrated Circuits Symp. Dig.*, 2009; 469–472.
21. Li L, Reyneart P, Steyeart M. A Colpitts LC VCO with Miller-capacitance gm enhancing and phase noise reduction techniques. *Proc. of Europ. Solid-State Circuits Conf.* (*ESSCIRC*), 2011; 491–494.
22. Decanis U, Ghillioni A, Monaco E, Mazzanti A, Svelto F. A low-noise quadrature VCO based on magnetically coupled resonators and a wideband frequency divider at millimetre waves. *IEEE Journal of Solid-State Circuits* 2011; **46**(12):2943–2955.
23. Scheir K, Vandersteen G, Rolain, Wambacq P. A 57-to-66 GHz quadrature PLL in 45 nm digital CMOS. In *Int. Solid-State Circuits Conference*, 2009; 494–495.
24. Catli B, Hella MM. A 60 GHz CMOS combined mm-wave VCO/divider with 10-GHz tuning range. *IEEE Custom Integrated Circuits Conference* (*CICC*), 2009; 665–668.
25. Shirinfar F, Nariman M, Sowlati T, Rofougaran M, Rofougaran R, Pamarti S. A multichannel, multicore mm-wave clustered VCO with phase noise, tuning range, and lifetime reliability enhancements. *IEEE Radio Frequency Integrated Circuits Symposium* (*RFIC*), 2013; 235–238.
26. Xi T, Guo S, Gui P, Zhang J, Kenneth KO, Fan Y, Huang D, Gu R, Morgan M. Low-phase-noise 54 GHz quadrature VCO and 76 GHz/90 GHz VCOs in 65 nm CMOS process. *IEEE Radio Frequency Integrated Circuits Symposium*, 2014; 257–260.
27. Cao H, O KK. Millimeter-wave voltage-controlled oscillators in 0.13-µm CMOS technology. *IEEE Journal in Solid-State Circuits*, 2006; **41**(6):1297–1304.